Fracture Behavior in Cu46.5Zr46.5Al7 and Cu46.5Zr41.5Al7Y5 Bulk Metallic Glasses

Fracture behavior in $Cu_{46.5}Zr_{46.5}Al_7$ and $Cu_{46.5}Zr_{41.5}Al_7Y_5$ bulk metallic glasses

P. Matteis[a], P. Russo Spena[b], C. Pozzi[a], T.A. Baser[c,d], M. Baricco[c], L. Battezzati[c], D. Firrao[a], A. Castellero[c]

[a] DISMIC - Politecnico di Torino, Torino, Italy.

[b] DISPEA - Politecnico di Torino, Torino, Italy.

[c] Dipartimento di Chimica IFM and NIS, Università di Torino, Torino, Italy.

[d] Laboratory for Joining Interface and Technology, EMPA, Dübendorf, Switzerland.

Abstract

The interplay between chemical composition, plastic behavior, and fracture modes of $Cu_{46.5}Zr_{46.5}Al_7$ and $Cu_{46.5}Zr_{41.5}Al_7Y_5$ bulk metallic glasses was investigated by compression tests and fracture surfaces analyses. The aim was to explore the possibility of coupling physical, chemical and hardness properties, with adequate macroscopic compressive plasticity.

Cylindrical test samples, having a height-to-diameter ratio equal to 2, were machined and ground from as-cast bars and were tested in compression between lubricated plates, the displacement being measured by a clip-gage inserted between the plates.

Y free BMG engineering stress-strain curves show a plastic behavior consisting of successive sudden stress drops and linear reloading segments. A detailed analysis of these features was performed to yield a correlation between the plastic deformation steps and the released elastic energy associated with each serration.

Introduction

In early studies, metallic glasses could only be produced at very high cooling rates that could be obtained by casting very thin sections, e. g. ribbons less than 0.1 mm thick. These could not be characterized by the usual mechanical testing procedures.

More recently, alloys with slower crystallization kinetics have been developed, allowing the production of bulk samples of metallic glass. In particular, several investigations focused on the Cu-Zr system; Bulk Metallic Glass (BMG) bars with diameter up to 10 mm were fabricated [1,2].

Owing to the absence of dislocations, BMGs exhibit a nearly theoretical strength before failure [3], yet with a very low ductility at room temperature. In fact, under uniaxial compressive loading at room temperature, most BMGs show a macroscopically brittle behavior [4], with very low plastic strain (< 2 %). This is due to a highly localized deformation process, i.e. shear banding [5], whereby a large plastic strain occurs in a narrow layer exhibiting strain (or thermal) softening [6-10], which leads to failure. When BMGs show a larger overall plastic deformation at room temperature, the plastic flow is often discontinuous, as evidenced by serrated stress-strain curves, with repeated stress drops [11]; each serration may correspond to the activation of a weak shear band, which soon ceases to operate [11].

The BMGs yielding behavior is sensitive to the hydrostatic component of the stress tensor, and is often described by a Mohr-Coulomb yield criterion; in particular, the internal friction coefficient can be calculated from the observed orientation of the shear plane in respect to the loading axis [12-16].

The main goal in toughening BMGs is to prevent a single shear band from going through

the whole sample, and to promote, instead, the formation of multiple shear bands. The toughness of BMGs, and hence their ductile/brittle behavior, is related to the ratio μ/B where μ is the elastic shear modulus, and B is the bulk elastic modulus, or, equivalently, to the Poisson ratio, ν [17]. The lower the μ/B ratio, the higher is the fracture energy. In particular, glasses based on Cu, Zr, Pt, or Pd, having low μ/B ratios, exhibit a high density of shear bands [17-19] and have microscopically ductile vein-pattern fracture surfaces [17,18]. Hence, the BMGs intrinsic ductility may be enhanced by careful chemical design, i.e. by choosing alloying elements on the basis of their likely effects on the elastic constants [17,20,21]. Moreover, an increase in toughness can be obtained by extrinsic techniques such as the *in situ* formation of a crystalline second phase, which promotes the formation of multiple shear bands via mismatch of various properties and, in the meantime, prevents their propagation, thus resulting in enhanced macroscopic ductility [17].

The mechanical properties of Cu-Zr-Al BMGs have been extensively studied; in particular, several BMGs derived from the $Cu_{50}Zr_{50}$ system with minor Al additions show significant plastic deformation at room temperature [22]. The mechanical behavior of $Cu_{50-x/2}Zr_{50-x/2}Al_x$ BMGs has been related to the amount of nanoscale crystalline precipitates [23], which generally occur in $Cu_{50}Zr_{50}$ [5], but are increasingly suppressed by the addition of Al [24,25], a fully amorphous structure being expected for 7 %at. Al [26]. The precipitates are believed to promote the nucleation of multiple shear bands, which hinders their fast propagation, leading to relatively large ductility [5], whereas a fully amorphous phase allows a fast shear band propagation, leading to a more brittle behavior.

Recent successful attempts to improve the plasticity of Cu-Zr-Al BMGs were made by introducing micron-sized second phase particles, such as B2-$Cu_{50}Zr_{50}$, by controlled cooling [27]. In the binary Cu-Zr phase diagram the B2-$Cu_{50}Zr_{50}$ phase is stable above 985 K [28] and, upon cooling, tends to transform to a monoclinic martensitic phase (B19'), metastable at room temperature [29]. The addition of Al to Cu-Zr promotes the stabilization of the B2-$Cu_{50}Zr_{50}$ phase which can be retained at room temperature by applying suitable cooling rates [30]. The increased plasticity of these Cu-Zr-Al composites with respect the corresponding monolithic BMGs can be ascribed to the presence of the B2-$Cu_{50}Zr_{50}$ micron-sized particles. On the one hand, since the elastic properties of B2-$Cu_{50}Zr_{50}$ are very similar to those of the Cu-Zr-Al amorphous matrix, no local stress concentration arises at the crystal/glass interface during compression and the second phase particle can accommodate the strain due to its ductility [27]. On the other hand, the observed deformation induced transformation from B2 to B19' seems to cause a remarkable compressive work-hardening of the alloys containing a crystalline volume fraction higher than 40 % [31].

The fracture strains of the Cu-Zr(-Al) BMGs usually show a large scatter, being in part probably intrinsic and in part arising from different casting conditions, which may influence the local microstructure and particularly the presence of nano-sized inhomogeneities. Thus, large differences can be observed among samples with various diameters prepared in different laboratories (e.g. from 4 to 12 % for $Cu_{50}Zr_{50}$ [26,32]) and even among different positions in the same cast sample.

The fracture behavior of a fully amorphous $Cu_{46.5}Zr_{46.5}Al_7$ alloy and of a partially crystalline $Cu_{46.5}Zr_{41.5}Al_7Y_5$ alloy was investigated in this work by performing series of

monotonic compression tests, with either quasi-static (10^{-4} s^{-1}) or dynamic (1 s^{-1}) deformation velocities.

Experimental

Specimen preparation

The $Cu_{46.5}Zr_{46.5}Al_7$ and $Cu_{46.5}Zr_{41.5}Al_7Y_5$ glass-forming alloys, herein indicated as alloy A or B, respectively, were cast under vacuum in a vertical, 3 mm diameter cylindrical copper mold, with a riser cone on top, yielding one blank bar for each alloy. XRD analyses, performed by using Cu radiation and with a Bragg-Brentano setup (Fig. 1), on 1 mm thick slices, show that the alloy A bar was fully amorphous, whereas the alloy B bar was partially crystalline, with XRD peaks due to the B2-$Cu_{50}Zr_{50}$ type phase, whose lattice constant, *a*, was estimated to be 0.3288 nm. The value found here is larger than the one accepted for the binary stoichiometric compound (*a* = 0.3262 nm, [28]), indicating the probable presence of certain amount of Y since this element tends to expand the unit cell. In fact, the isostructural compound B2-$Cu_{50}Y_{50}$ has a lattice constant of 0.3479 nm [33]. As already mentioned in the introduction, the B2 is known to be stable at high temperature, and it likely grew from the liquid. Ensuing metallographic examinations, performed by SEM upon polished and etched (aqueous solution of 20 % HF and 1 % HNO_3) cross-sections, showed that the microstructure of the B bar consisted of a continuous amorphous phase with isolated CuZr dendrites; the latter were 10 to 15 μm wide and were often (but not always) aligned in long rows. DSC (differential scanning calorimetry) analyses allowed to estimate that the crystalline phase fraction was 13 ± 2 %vol.

A series of cylindrical compression specimens was machined from each as-cast bar; 0.01 mm planarity, cylindricity and perpendicularity tolerances were ensured after grinding of all the specimens surfaces. A small crystalline phase fraction was found by XRD on the as-grinded surfaces of the alloy A specimens, probably due to a localized thermal effect of the grinding procedure; however, no crystalline phases were detected after a slight polishing of the same surfaces, confirming that the bulk material was indeed fully amorphous. The specimens were progressively numbered from the bottom end of each bar (opposed to the riser cone), from A1 to A7 and from B1 to B6.

Compression tests and data analysis techniques

In the compression tests, the specimens were loaded between a couple of high C tool steel plates (about 14 x 12 mm wide and 4 mm thick) in a servohydraulic universal testing machine. In order to avoid any significant plastic deformation of the plates, the plates were much harder than the samples (~840 vs. ~560 HV_{100}). The contact between the specimen and the compression plates was lubricated with a dry graphite lubricant, with 0.123 nominal friction coefficient, sprayed upon the plates before each test. The load was measured by a remote load cell, and the displacement by a clip gage mounted between the plates, a few millimeters away from the load line. Therefore, the instantaneous specimen height, h, was the sum of the length measured by the clip gage, y, and of the two plates elastic displacement, $2\cdot\delta$. The latter was computed with the Boussineq solution for an elastic half-space indented by a rigid cylinder, that is: $\delta = (P/d)\cdot((1-\nu^2)/E)$, where d is the cylinder diameter, P is the instantaneous load and E and ν are the Young's modulus and Poisson ratio, respectively. Thus, the instantaneous specimen height was $h = y + 2\cdot\delta$

= y + 2·(P/d)·((1-ν^2)/E). In this calculation, the instantaneous specimen diameter d was replaced by its initial value d_0 (the difference being negligible), and the steel plates E and ν elastic constants were assumed to be 210 GPa and 0.3, respectively. The engineering and true stress-strain curves were then calculated in the usual manner from the h, h_0, P and d_0 values. It should be noted that this test geometry causes an inhomogeneous stress distribution on the contact area between the plate and the sample, with the maximum stress on the specimen edge (as first noted in the same Boussineq solution), and that this stress distribution may be further modified by possible alignment errors; these facts were neglected in the present calculations, even if the edge stress concentration was recently found to influence the fracture location in BMG specimens subjected to dynamic loading at very high strain rates [34].

The estimated compliance of the specimen (obtained from the typical specimen dimensions ad elastic modulus), of the two plates (due to the local elastic deformation and obtained from the above formulas for the typical specimen diameter) and of the load frame (obtained from the actuator displacement vs. load curve recorded by pressing the compression fixtures one against the other without the specimen) were about 12, 3 and 7 μm/kN, respectively.

The specimens were loaded under actuator displacement control, and the actuator speed, constant during each test, was chosen in order to obtain specimen strain rates close to either 1 s^{-1} (dynamic tests) or 10^{-4} s^{-1} (quasi-static tests). Dynamic tests were performed on the A1, A4, B1 and B4 specimens, and quasi-static tests on all the other specimens. In the case of A6 and B2 quasi-static tests the strain rate was slightly different, i.e. close to $0.5 \cdot 10^{-4}$ and $2 \cdot 10^{-4}$ s^{-1}, respectively.

The sampling rate for data acquisition (constant during each test) was adequate in the quasi-static tests, but in the dynamic tests corresponded (in the elastic range) to only 1 point every about 100 MPa.

After the initial linear-elastic part, the engineering stress-strain curves of the A-series specimens showed several successive serrations, each consisting of a sudden stress drop and strain increment followed by an almost linear re-loading segment extending up to the following stress drop. These serrations were further examined with the following procedure.

- Stress-drops were identified as the data points following the point-to-point stress and strain variations larger than $4\Delta s$ and Δe, respectively. Δs and Δe were defined respectively as the minimum point-to-point stress variation (negative) and the maximum point-to-point strain variation (positive) found in the linear-elastic part of the stress-strain curve.
- Each re-loading segment, comprised between successive stress drop points (or after the last one), was linearly interpolated, using the stress as the independent variable. A reference strain distance was calculated between each pair of successive re-loading interpolating lines, corresponding to the mean value of the overlapping stress range of the two re-loading segments. A stress drop was considered valid only if its corresponding reference strain distance was larger than Δe. The interpolations were then repeated, if necessary, considering the confirmed stress drops only.
- The stress/strain slope $E_r^{(i)}$ of each i-th re-loading segment was obtained from its linear interpolation; the apparent plastic deformation increment $\Delta e_p^{(i)}$, associated to each i-th stress drop, was calculated as the strain distances between the two

successive re-loading segments corresponding to the higher limit of their overlapping stress range. The apparent elastic energy density drop $\Delta U_{el}^{(i)}$, associated with each i-th stress drop, was calculated from the stress before and after the drop and from the specimen elastic modulus E.

This procedure was not applied to the dynamic test results, due to the low number of data. The angle γ between the loading axis and the overall fracture plane of the A-series specimens was measured on optical images of the broken specimens, acquired from a line of view perpendicular to the loading axis and lying into the fracture plane. The latter condition was the main uncertainty source, since fracture surfaces were only approximately planar; in some cases two images were taken from either slightly different or opposite directions of view.

Results

Mechanical test results

The microhardness of the two alloys was essentially equal, namely 565 ± 6 and 557 ± 5 $HV_{0.1}$ for the $Cu_{46.5}Zr_{46.5}Al_7$ and $Cu_{46.5}Zr_{41.5}Al_7Y_5$ alloys (mean ± standard deviation), respectively.

The overall compressive behavior is almost elastic-perfectly plastic. The elastic modulus E, the maximum true stress σ_{max}, and the maximum true strain ε_{max} do not show relevant variations, neither between alloys A and B, nor between the two strain rates (Table I). The dynamic σ_{max} values are indeed slightly smaller than the quasi-static ones, but the former may be underestimated due to the relatively low sampling rate. Moreover, no trend could be detected as a function of the original position in the cast bars (i. e. specimen number).

Table I – Monotonic compression test results: elastic modulus E, maximum true stress σ_{max}, maximum true strain ε_{max} (as recorded in the stress-strain curve), maximum true plastic strain $\varepsilon_{pl,max}$ ($\approx \varepsilon_{max} - \sigma_{max}/E$), number of linear re-loading segments N; mean values.

BMG	Loading Rate	Specimen values							Mean ± standard			
		#	E	σ_{max}	ε_{max}	$\varepsilon_{pl,max}$	N	γ	E	σ_{max}	ε_{max}	$\varepsilon_{pl,max}$
-	-	-	GPa	MPa	%	%	-	deg.	GPa	MPa	%	%
$Cu_{46.5}Zr_{46.5}Al_7$	Quasi-Static	A2	83.9	1869	2.63	0.40	16	n.a	87.0 ±5.9	1886 ±18	2.70 ±0.44	0.53 ±0.35
		A3	91.7	1895	2.33	0.27	8	46-43				
		A5	94.3	1897	2.52	0.51	14	41				
		A6	79.9	1863	3.46	1.13	41	n.a				
		A7	85.3	1905	2.56	0.32	4	41				
	Dynamic	A1	90.4	1799	2.60	0.61	n.a.	41	86.2 ±5.9	1808 ±12	2.47 ±0.18	0.36 ±0.34
		A4	82.0	1816	2.34	0.12	n.a.	39 - 43				
$Cu_{47}Zr_{42}Al_7Y_5$	Quasi-Static	B2	76.3	1899	3.59	1.10	0	n.a	80.4 ±4.7	1849 ±54	2.92 ±0.50	0.61 ±0.37
		B3	86.7	1833	2.51	0.40	0	n.a				
		B5	81.0	1883	3.03	0.71	0	n.a				
		B6	77.6	1781	2.55	0.25	0	n.a				
	Dynamic	B1	83.2	1667	2.11	0.11	n.a.	n.a	84.8 ±2.2	1740 ±103	2.42 ±0.44	0.37 ±0.37
		B4	86.4	1813	2.73	0.63	n.a.	n.a				

A number of linear re-loading segments (between 4 and 41) were detected in the $Cu_{46.5}Zr_{46.5}Al_7$ stress-strain curves, whereas generally none was found in the $Cu_{46.5}Zr_{41.5}Al_7Y_5$ stress-strain curves (Fig. 2a). Fig. 2b is a working example of the procedure used to identify and interpolate these re-loading segments.

The stress/strain slopes $E_r^{(i)}$ of the re-loading segments show a large dispersion (even if values obtained from segments with less than 10 data points were discarded), and no evident trend in respect to the re-loading sequence or to the specimen origin; nevertheless, the $E_r^{(i)}$ (mean ± standard deviation 80.0 ± 15 GPa) range roughly overlaps that of the elastic modulus E values (87.0 ± 5.9 GPa) measured in the same tests.

The apparent drops of elastic energy per unit volume (ΔU_{el}) occurring during each stress drop show a linear correlation with the apparent plastic deformation increments Δe_p, considering a relationship of the form $\Delta U_{el} = \beta \Delta e_p$. It can be found that $\beta = 800$ mJ/mm^3 (Fig. 2c).

Fractography

All the A ($Cu_{46.5}Zr_{46.5}Al_7$) specimens broke in two fragments, separated by an oblique plane which, in 6 out of 7 cases, was tangent to one specimen edge, probably due to the already mentioned edge stress concentration. The overall mean value of the γ angles (Table I) is 42° and, assuming a Mohr-Coulomb yield criterion, corresponds to an internal friction coefficient $\alpha_n = 0.11$. This is consistent with previous results, regarding both the influence of the edge stress concentration [34] and the Mohr -Coulomb yield criterion [12-15].

On the contrary, all the B ($Cu_{46.5}Zr_{41.5}Al_7Y_5$) specimens broke in a large number of small fragments; this can be classified as a "fragmentation fracture", previously found in several BMGs and recently studied in more detail [35,36]; even if this type of fracture has not been completely understood yet, it is believed that dynamic effects (i.e. shock waves triggered by the earlier fracture events) play a major role, and that the fracture can take place under local tensile stresses [36].

The fracture surface of the examined $Cu_{46.5}Zr_{46.5}Al_7$ A7 specimen consists almost completely of a single shear fracture plane (Fig. 3a), showing the vein-like pattern (Fig. 3b). A vein pattern is generally believed to be formed by the viscous flow occurring in a thin layer (shear band) of material softened (or even melted, in the final fracture stage

[37]) by the heat produced by localized shear deformation. A handful of intersection between the dominant strong shear fracture plane and other minor ones are also detected, appearing as surface steps with secondary cracks on part of their edges (Fig. 3c,d). In most cases the vein pattern seems to continue through the step edges. In one case, apparently melted and resolidified material is found at the opening of a secondary crack (Fig. 3c), which is probably the opening of an intersecting minor shear band. It may be concluded that this was formed by material melted in the minor shear band and then spilled out (and resolidified) when the latter was cut by the dominant fracture surface. This would be consistent with previous observation of both large temperature rise and melting on BMGs' fracture surfaces [8-10]. Finally, in one case a series of apparent shear bands are found close to the tip of a secondary crack (Fig. 3d), being superimposed to the vein pattern. A tentative interpretation is that the deformation marks formed in the crack-tip stress field of the minor crack when the material was still sufficiently hot to deform plastically, the heat having been released by the main shear deformation band that caused the fracture.

The fracture surface of the examined $Cu_{46.5}Zr_{41.5}Al_7Y_5$ B2 specimen consists of facets of unequal dimension and orientation (Fig. 4a,b), often separated by secondary cracks (Fig. 4b). These facets in most cases show either a corrugated pattern with roughly aligned relief features (Fig. 4c, top and left), or a pattern consisting of smooth areas separated by ridges and of protruding dimpled cones, generally situated at ridge ends (Fig. 4c, bottom and right). The smooth areas outlined by the ridges often exhibit smaller surface steps (river lines), resembling the well-known mirror-mist-hackle fracture, which is common in non-metallic glasses [38] and has been recently observed in the fragmentation fracture of

Co-based BMGs [35]. A tentative interpretation is that the latter smooth pattern arises from a normal (mode I) opening, and the dimpled cones are the trace of the last elongated ligaments, whereas the former corrugated pattern arises from a shear (mode II) opening, with relief features aligned in the shear direction; intermixed mode I and mode II opening areas can be found in the same fracture surface due to the fragmentation fracture process. The origin of the dimpled cones was investigated by performing polished and etched cross sections perpendicular to the fracture surfaces (Fig. 4d); it was ascertained that the dimpled cones correspond to the CuZr dendrites, thus implying that the latter ones constitute the more ductile cones.

Discussion

The serrated flow observed in the $Cu_{46.5}Zr_{46.5}Al_7$ (alloy A) BMG tested in compression are consistent with similar phenomena previously noted in several BMGs of different compositions [16,39]. In particular, the reloading slope is on average close to the elastic modulus, notwithstanding a very large dispersion; therefore, it is concluded that the overall plastic deformation is formed by a series of discrete deformation bursts, alternated with intervals of elastic behavior. Each deformation event may thus correspond to the transitory activation of a shear band.

The energy per unit volume irreversibly absorbed by the specimen during each of these events is theoretically equal to the product of the (mean) flow stress and of the plastic deformation increment. This correspond to the energy density drops plotted in Fig. 2c as a function of the extent of individual increments. The straight line representing the ensemble of points has slope of 800 mJ/mm^3. This figure expresses the volumetric energy

density per unit deformation. The deformation here is only apparently plastic since the overall elongation is actually due to several elastic serrations each followed by a stress drop. Remembering that the elastic deformation before yielding is around 2.3 %, the above figure corresponds well to the actual flow stress of the order of 1850 MPa.

Let us consider now the set of ΔU values in the ordinate of Fig. 2c going from $4.75 \cdot 10^5$ Jm^{-3} to $5 \cdot 10^4$ Jm^{-3}. These are computed with reference to the volume of the sample (30.9 mm^3) and, therefore, correspond to absolute values of energy from $1.47 \cdot 10^{-2}$ J to $1.54 \cdot 10^{-3}$ J. Assuming that serrations occur because of activation of shear bands and recalling that according to Lewandowski and Greer [9] the energy content of a shear band in a Zr-based alloy is of the order of 2000 Jm^{-2}, it is deduced that the extremes of the ΔU values must refer to areas of 7 mm^2 and 0.8 mm^2, respectively. The cylinders used for testing in the present work have areas of 5.72 mm^2. Supponing that the shear band moves on a plane with the same 42° inclination with respect to the compression axis, the area it can span is 10.3 mm^2. Therefore, in correspondence to the higher amounts of energy release, the shear band should extend to a substantial part of the sample whereas for the lower amounts here detected it will span less than one tenth of the sample.

The hardness and the compressive strength in the two examined alloys of the Cu-Zr-Al system are almost equal, notwithstanding the CuZr crystalline phase fraction and the Y alloying addition of the B alloy; yet, as it regards the plastic strain-to-fracture, the possible differences among the two alloys could not be clarified due to the large data dispersion ($\varepsilon_{pl,max}$ varying from 0.25 to 1.10 %).

On the other hand, it was ascertained that either the Y addition, or the crystalline phase fraction, or both, suppress the occurrence of serrations in the stress-strain curve, and

modify the final fracture mode, yielding a large number of irregular fragments. Also the appearance of the fracture surface is modified, yielding both supposed mode-I (normal) and mode-II (shear) fracture opening areas, the former exhibiting dimpled cones generated upon fracturing the fracture of the crystalline phase. The lack of serrations suggests that the alloy B undergoes a more homogeneous deformation, which may arise from a much larger number of much smaller microscopic deformation events, none of which can be individually detected by the test apparatus here employed.

The fragmentation fracture behavior of the Y alloyed material may derive from different causes, including its microstructural inhomogeneities; e.g., the formation of the crystalline phase may have been associated with free-volume inomogeneities in the amorphous matrix, which in a recent study on Co-based BMGs has been proposed as possible multiple crack initiation sites causing a fragmentation fracture [40].

Conclusions

The $Cu_{46.5}Zr_{46.5}Al_7$ BMG tested in compression exhibit an almost elastic – perfectly plastic behavior, with a limited plastic deformation (up to 0.015) occurring through a series of discrete deformation bursts (serrations), each attributed to the transitory activation of a shear band. The fracture strength is close to 1850 Mpa. The fracture occurs on one dominant shear plane, showing a vein-like pattern. However, minor shear bands also occur and can be cut through by the dominant shear plane; these shear band intersections can be decorated by melted and resolidified material, which probably melts inside the minor band and then spills out and resolidified when the same band is cut; this phenomenon is consistent with previous observation of both large temperature rise and

melting on BMGs' fracture surfaces.

Careful analysis of the serrations obtained during deformation of the ternary amorphous alloys allows to estimate their energy content and relate it to the portion of the sample where the shear band operates.

The partially crystalline $Cu_{46.5}Zr_{41.5}Al_7Y_5$ BMG does not show serrations, and exhibit a fragmentation fracture with distinctly different fracture surface morphologies (with supposed mode-I normal and mode-II shear opening regions); hence it is hypothesized that in this alloy a larger number of weaker shear bands, none of which becomes dominant, are produced.

Acknowledgements

The authors would like to express their appreciation to Prof. Jürgen Eckert and Dr. Jayanta Das for the useful discussions and the help in sample preparation. This program was supported by the Regione Piemonte (Italy) under contract D-23.

References

[1] D. Xu, G. Duan, W. L. Johnson, Phys. Rev. Lett. 92 (2004) 245504.

[2] G.Q. Zhang, Q.K. Jiang, L.Y. Chen, et al., J. All. Comp. 424 (2006) 176.

[3] A.L. Greer, Science 267 (1995) 1947.

[4] J. Das, M.B. Tang, K.B. Kim, et al., Phys. Rev. Lett. 94 (2005) 205501.

[5] J. Eckert, J. Das, K.B. Kim, et. al., Intermetallics 14 (2006) 876.

[6] H. J. Leamy, H. S. Chen, T. T. Wang, Metall. Trans. 3 (1972) 699.

[7] H. Chen, Y. He, G.J. Shiftlet, et al., Nature 367 (1994) 541.

[8] B. Yang, P.K. Liaw, G. Wang et al., Intermetallics 12 (2004) 1265.

[9] J.J. Lewandowski, A.L. Greer, Nature Materials 5 (2006) 15.

[10] Y.Zhang, N.A. Stelmashenko, Z.H. Barber et al., J. Mater. Res. 22 (2007) 419.

[11] A.R. Yavari, J.J. Lewandowski, J. Eckert, MRS Bulletin, 32 (2007) 635.

[12] L.A. Davis, S. Kavesh, J. Mater. Sc. 10 (1975) 453.

[13] P.E. Donovan, Acta Metall. 37 (1989) 445.

[14] P. Lowhaphandu, S.L. Montgomery, J.J. Lewandowski, Scripta Materialia 41 (1999) 19.

[15] J.J. Lewandowski, P. Lowhaphandu, Philos. Mag. A 82 (2002) 3427.

[16] C.A. Schuh, T.C. Hufnagel, U. Ramamurty, Acta Mater. 55 (2007) 4067.

[17] J.J. Lewandowski, M. Shazly, A.S. Nouri, Scripta Mater. 54 (2006) 337.

[18] J.J. Lewandowski, W.H. Wang, A.L. Greer, Phil. Mag. Lett. 85 (2005) 77.

[19] J. Schroers, W.L. Johnson, Phys. Rev. Lett. 93 (2004) 255506.

[20] J.J. Lewandowski, X.J. Gu, A. Shamimi Nouri, et al., App. Phys. Lett. 92(9) (2008) 09198-1.

[21] A. Shamimi Nouri, X.J. Gu, S.J. Poon, et al., Phil. Mag. Lett. 88(11) (2008) 853.

[22] D.S. Sung, O.J. Kwon, E. Fleury, et al., Metals Mater. Int. 10 (2004) 575.

[23] T.A. Baser, J. Das, J. Eckert, et al. J. All. Comp., to appear in proc. ISMANAM-2007.

[24] A. Inoue, W. Wang, Mater. Trans., 43 (2002) 2921.

[25] K.B. Kim, J. Das, F. Baier, et al., Appl. Phys. Lett 88 (2006) 051911.

[26] S.W. Lee, M.Y. Huh, E. Fluery, et al., Acta Mater. 54 (2006) 349.

[27] S. Pauly, G. Liu, G. Wang, U. Kühn, N. Mattern and J. Eckert, *Acta Mater.* **57** (2009)

5445.

[28] E.M: Carvalho and I.R. Harris, *J. Mater. Sci.* **15** (1980) 1224.

[29] A.W. Nicholls, I.R. Harris and W. Mangen, *J. Mater. Sci. Lett.* **5** (1986) 217.

[30] F. Jiang, Z.B. Zhang, L. He, J. Sun, H. Zhang and Z.F. Zhang, J. Mater. Res. 21 (2006) 2638.

[31] S. Pauly, J. Das, J. Bednarcik, N, Mattern, K.B. Kim, D.H. Kim and J. Eckert, *Scripta Mater.* **60** (2009) 431.

[32] Z.W. Zhu, H.F. Zhang, W.S. Sun, et al., Scripta Mater. 54 (2006) 1145.

[33] Pearson's Handbook of Crystallographic Data for Intermetallic Phases, P. Villars and L.D. Calvert editors, American Society for Metals, Metals Park, OH, 1985, p. 2039.

[34] G. Sunny, J. Lewandowski, V. Prakash, J. Mater. Res. 22 (2007) 389.

[35] Z. F. Zhang, H. Zhang, B. L. Shen et al., Phil. Mag. Lett. 86 (2006) 643-650.

[36] J.X. Zhao, R.T. Qu, F.F. Wu et al. J. App. Phys. 105 (2009) 103519.

[37] L. Battezzati, D. Baldissin, Scripta Mat., 59 (2008) 223.

[38] D. Hull, Fractography, Cambridge University Press, 1999, pp. 121-123.

[39] W.J. Wright, R.B. Schwarz, W.D. Nix, Mater. Sc. Eng. A 319-321 (2001) 229.

[40] J.T. Fan, Z.F. Zhang, S.X. Mao et al., Intermetallics 17 (2009) 445.

List of figures' captions

Fig. 1. X-ray diffractograms of the fully amorphous Cu46.5Zr46.5Al7 alloy (a) and of the partially crystalline Cu46.5Zr41.5Al7Y5 alloy (b), the latter showing diffraction peaks belonging to the CuZr phase.

Fig. 2. Quasi-static compression tests. Detail of the engineering curves of a $Cu_{46.5}Zr_{46.5}Al_7$ and a $Cu_{46.5}Zr_{41.5}Al_7Y_5$ specimens (a), identification and interpolation of the reloading segments in the $Cu_{46.5}Zr_{46.5}Al_7$ tests (b), relationship between apparent elastic energy density drops $\Delta U_{el}^{(i)}$ and apparent plastic deformation increments $\Delta e_p^{(i)}$ (c).

Fig. 3. Fracture surface of the $Cu_{46.5}Zr_{46.5}Al_7$ A7 specimen after quasi-static monotonic compression test. Overall view (a) and typical vein-like pattern (b). Isolated shear band intersections: with melted and resolidified material (c); with deformation lines apparently superimposed on the vein pattern (d).

Fig. 4. Fracture surface of the $Cu_{46.5}Zr_{41.5}Al_7Y_5$ B3 specimen after quasi-static monotonic compression test. Low magnification overall view (a); typical pattern at increasing magnifications (b,c) with supposed mode I (c, top) and mode II (c, bottom) fracture areas; polished and etched cross section cut trough a mode II fracture area (d).

Figure 1

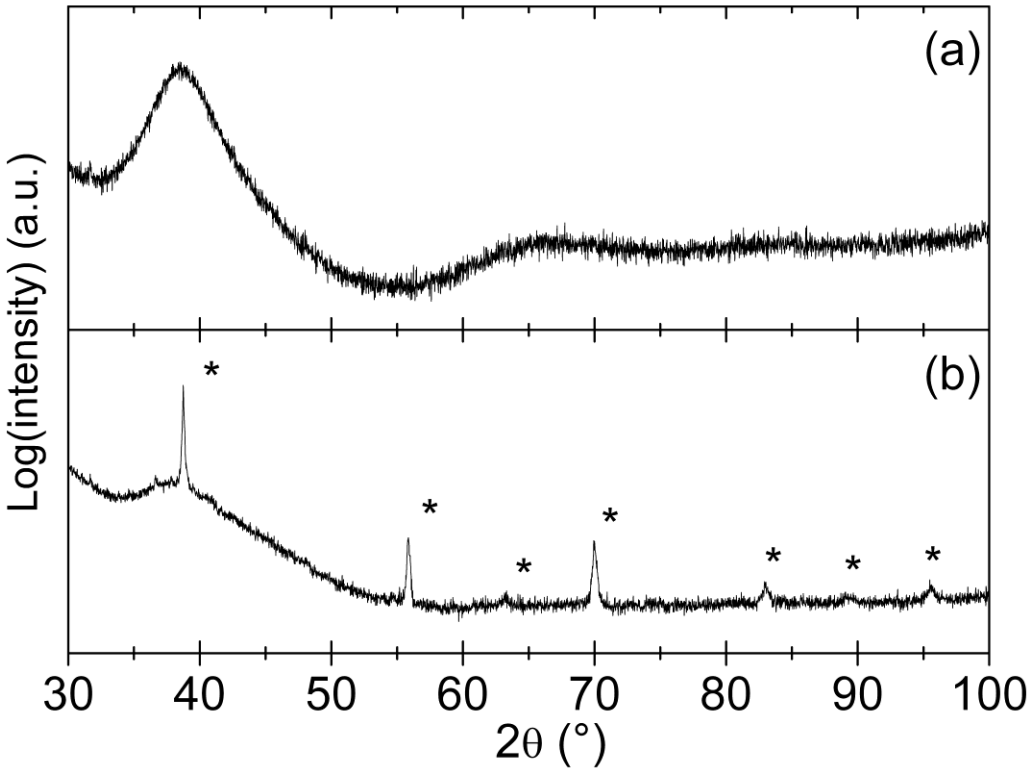

Figure 2(a)

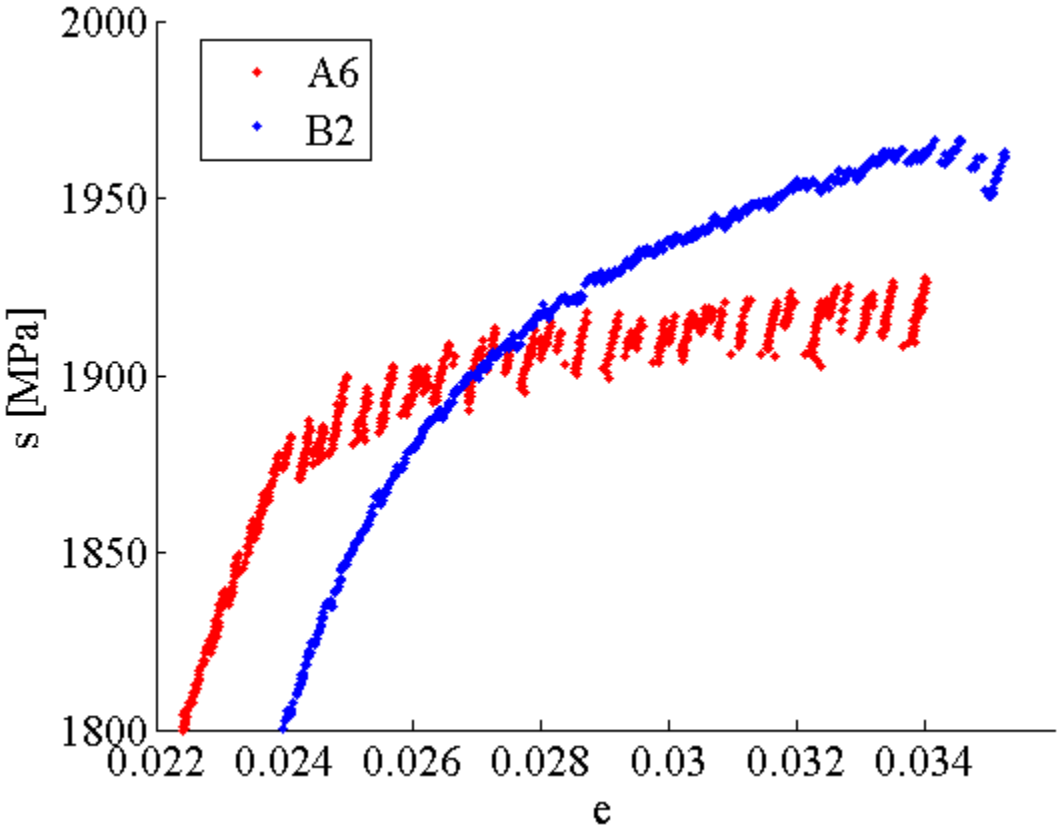
A6
B2
2000
1950
1900
1850
1800
s [MPa]
0.022
0.024
0.026
0.028
0.03
0.032
0.034
e

Figure 2(b)

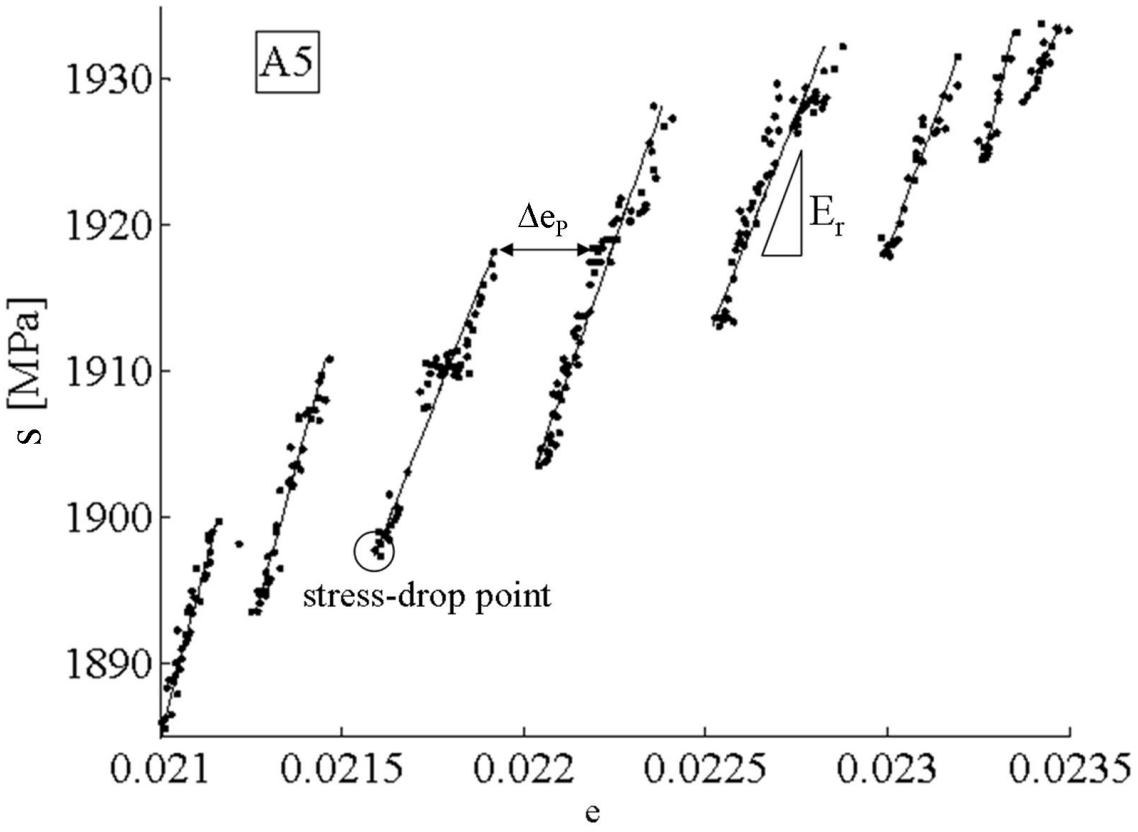
A5
1930
1920
1910
1900
1890
s [MPa]
Δe_P
E_r
stress-drop point
0.021
0.0215
0.022
0.0225
0.023
0.0235
e

Figure 2(c)

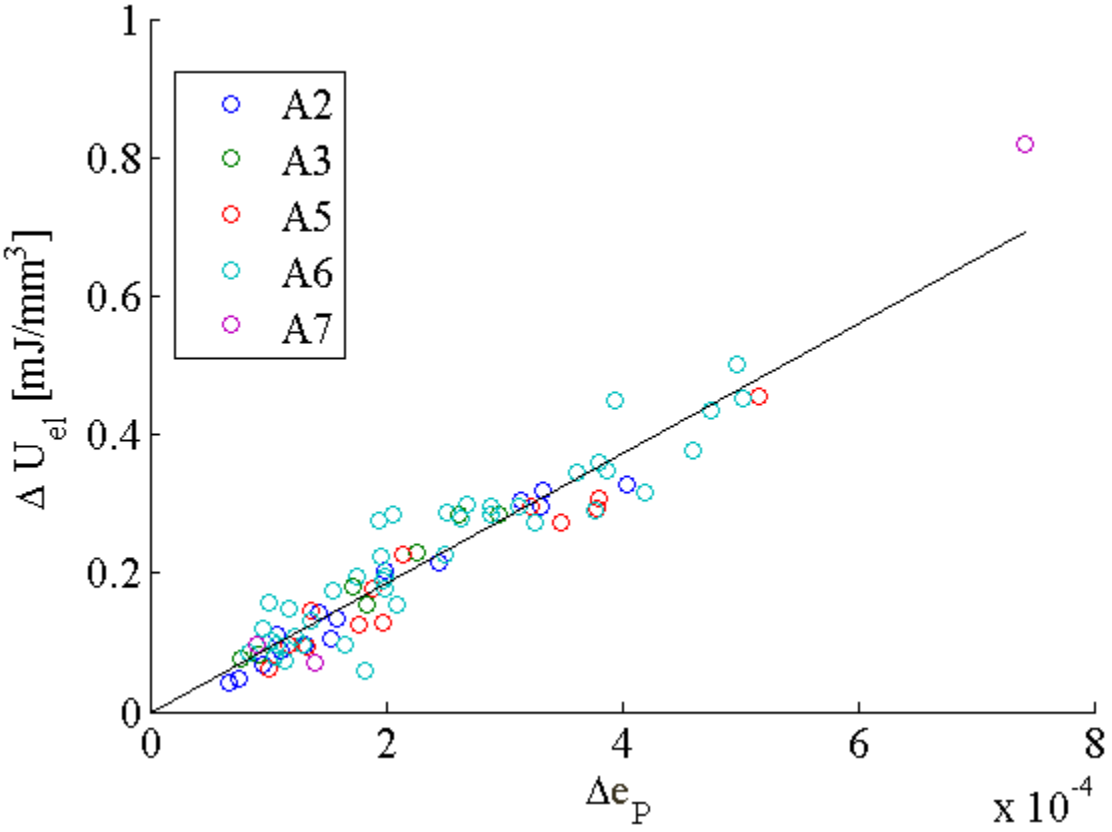

Figure 3

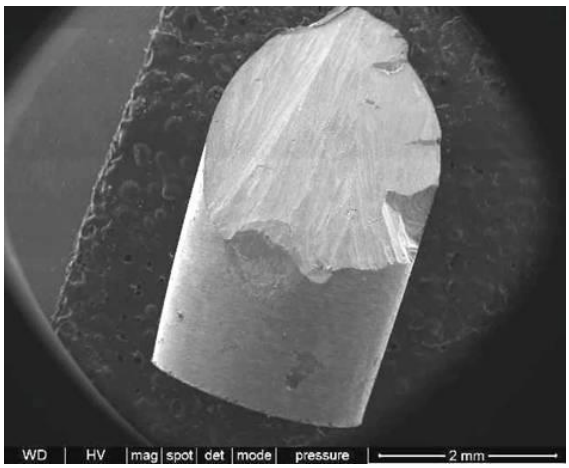

(a)

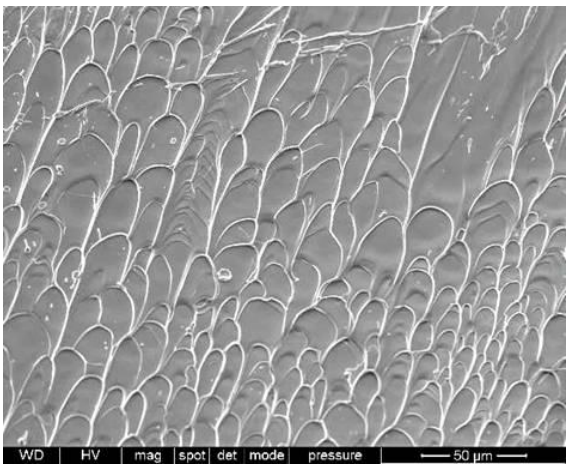

(b)

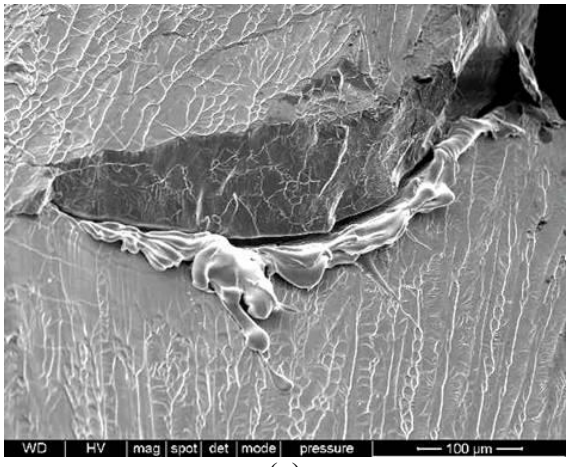

(c)

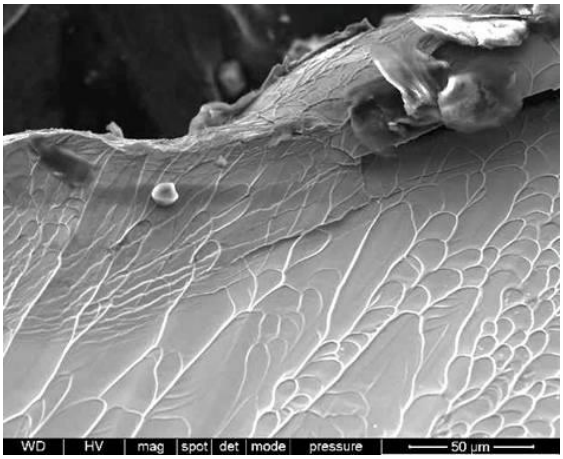

(d)

Figure 4

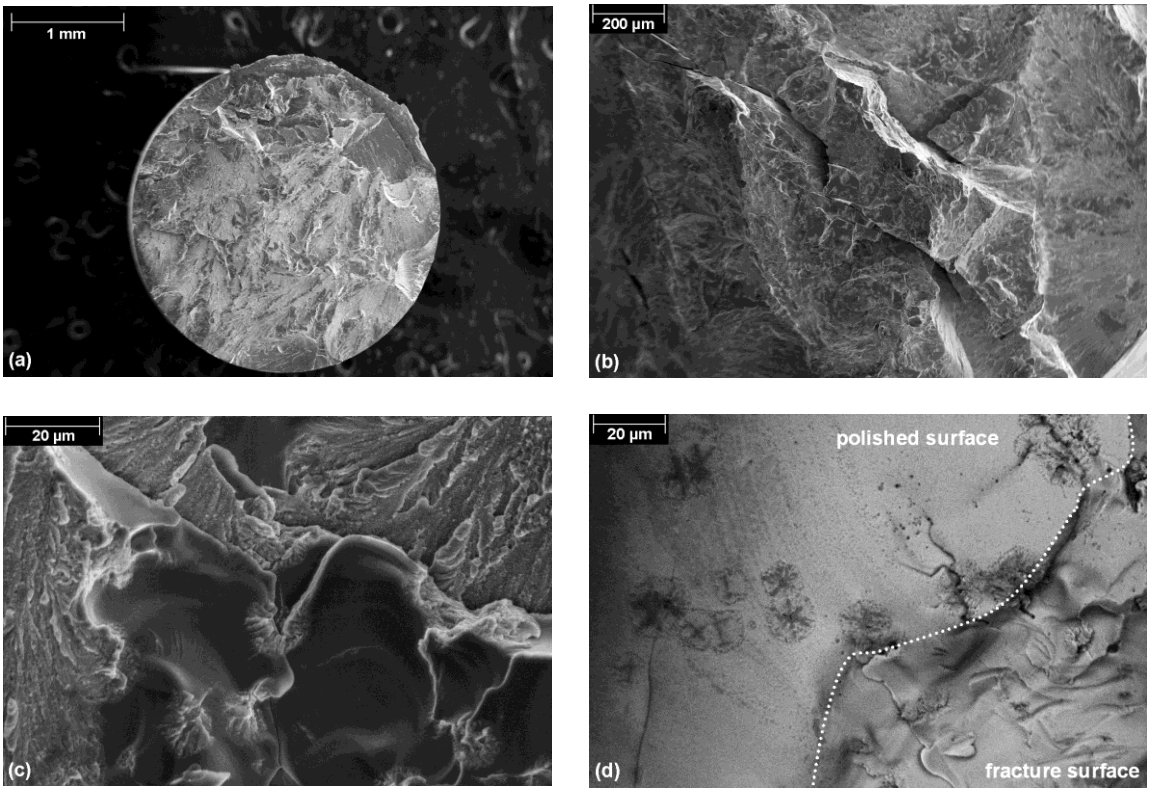
1 mm
(a)
200 µm
(b)
20 µm
(c)
20 µm
polished surface
(d)
fracture surface